Nanoscale

Tuning Dimensional Order in Self-Assembled Magnetic Nanostructures: Theory, Simulations, and Experiments

Journal:	*Nanoscale*
Manuscript ID	NR-ART-12-2023-006299.R2
Article Type:	Paper
Date Submitted by the Author:	01-Mar-2024
Complete List of Authors:	Chen, Yulan; Cornell University, Materials Science and Engineering Zhang, Hanyu; Cornell University, Applied and Engineering Physics El-Ghazaly, Amal; Cornell University, School of Electrical and Computer Engineering

Journal Name

ARTICLE TYPE

Cite this: DOI: 00.0000/xxxxxxxxxx

Tuning Dimensional Order in Self-Assembled Magnetic Nanostructures: Theory, Simulations, and Experiments†

Yulan Chen,*[a], Hanyu Alice Zhang,[b] and Amal El-Ghazaly*[c]

Received Date
Accepted Date

DOI: 00.0000/xxxxxxxxxx

A major obstacle to building nanoscale magnetic devices or even experimentally studying novel nanomagnetic spin textures is the present lack of a simple and robust method to fabricate various nano-structured alloys. Here, theoretical and experimental investigations were conducted to understand the underlying physical mechanisms of magnetic particle self-assembly in zero applied magnetic field. By changing the amount of NaOH added during the synthesis, we demonstrate that the resulting morphology of the FeCo assembly structure can be tuned from zero-dimensional (0D) nanoparticles to one-dimensional (1D) chains, and even three-dimensional (3D) networks. Two numerical simulations were developed to predict aspects of the nanostructure formation by accounting for the magnetic interactions between individual magnetic nanoparticles. The first utilized the Boltzmann distribution to determine the equilibrium structure of a nanochain, iteratively predicting the local deviation angle θ of each particle as it attaches to a forming chain. The second simulation illustrates the differences in nanostructure arrangement and dimensionality (0D, 1D, or 3D) that arise from random interactions at various nanoparticle densities. The simulation results closely match the experimental findings, as seen from SEM images, demonstrating their ability to capture the system's structural properties. Additionally, magnetic hysteresis measurements of the samples were taken along two orthogonal directions to show the influence of dimensional-order on the magnetic behavior. The normalized remanence ($M/M_{S\|}$) of the FeCo alloys increases as the dimensions of nanostructures are increased. Of the three cases, the FeCo 3D network structures exhibit the highest normalized nanostructure remanence of 0.33, and increased coercivity to above 200 Oe at 300 K. This combined numerical and experimental investigation aims to shed light on the preparation of FeCo nanostructures with tailorable dimensional order and open new avenues for exploring the complex spin textures and coercive behavior of these multi-dimensional nanomagnetic structures.

1 Introduction

Bottom-up self-assembly has emerged as a powerful strategy for organizing nanoscale building blocks into well-ordered supercrystals or superstructures.[1–3]. These self-assembled materials possess remarkable collective properties due to the synergistic interactions among individual building blocks, leading to enhanced optical[4], plasmonic[5], catalytic[6], electronic[7], magnetic[8–11], thermal[12], and mechanical[13] characteristics. In particular, the self-assembly of magnetic nanoparticles (MNPs) offers an intriguing avenue to harness magnetism as an additional degree of freedom in magneto-composites fabrication[14].

Experimental approaches have been employed to induce the self-assembly of diverse magnetic nanoparticle structures such as chains, rings, clusters, and supercrystals[15–17]. These strategies primarily rely on controlling magnetic interactions through the application of external magnetic fields[18,19]. Despite having the usage of external magnetic fields in common, understanding and replicating the underlying mechanisms of these self-assembly approaches remains challenging due to the complex interplay between intrinsic and extrinsic forces. Recent studies have revealed that self-assembly can occur through inherent magnetic interactions, even in the absence of external magnetic fields[20–22]. Moreover, several measurements[23–25] have provided evidence that the resulting magnetic properties critically depend on the configurations of the nanoparticles in the final structures. These findings have significantly contributed to our fundamental understanding of the magnetic properties exhibited by MNPs and their arrangements. While the self-assembly mechanisms involving MNPs con-

[a]Department of Materials Science and Engineering, Cornell University, Ithaca, New York 14853, USA. E-mail: yc2555@cornell.edu
[b]School of Applied and Engineering Physics, Cornell University, Ithaca, New York 14853, USA.
[c]School of Electrical and Computer Engineering, Cornell University, Ithaca, New York 14853, USA. E-mail: ase63@cornell.edu

† Electronic Supplementary Information (ESI) available. See DOI: 00.0000/00000000.

tinue to be elucidated, the reliable demonstration of self-assembly across all dimensional orders remains to be achieved.

Numerical studies have extensively explored the assembly of structures in magnetic colloidal systems using global energy minimization algorithms[26,27]. These simulations have taken into account various factors, such as the number of magnetic particles, their sizes, shapes, and dipolar orientations and interactions, leading to successful predictions of a diverse range of experimentally-observed ground states[28–30]. Furthermore, a recent simulation has examined the kinetic assembly path that sheds light on the possible trajectories of particles transitioning from a dispersed particle system to proposed ground state assembly structures[31]. Subsequent research has employed all-atom molecular dynamics to simulate the dynamics of more complex MNP systems in environments where hydrodynamic interactions caused by solvent molecules and ligands cannot be ignored[32]. However, it is important to note that these investigations have mainly focused on relatively static processes, examining stable configurations of aggregates formed with fixed particle numbers during fluid evaporation. These models did not consider the dynamic process of colloidal synthesis, where the nucleation rate governs the number of particles present in the system at a given time and influences the resulting final structure.

To address research gaps in the field, our study aims to demonstrate a synthetic pathway that enables the facile and versatile self-assembly of 0D MNPs into 1D and 3D architectures. Furthermore, we seek to simulate and investigate the influence of various parameters on the growth of individual nanoparticle chains, particularly focusing on the local tangent angles, and the resulting self-assembled structures. Our simulation approach involves two key aspects. First, we treat MNPs as colloidal monomers and draw parallels between the 1D assembly of MNPs and the process of monomer polymerization[33,34]. We utilize the worm-like chain (WLC) model from polymer physics to calculate the morphology of the 1D chain. This model assumes that the bending energy between adjacent polymer segments can adequately represent the statistical characteristics of chain conformation in polymers[35]. We systematically explore the impact of thermal energy and particle size, crucial factors determining chain morphologies. Our WLC model accurately captures the growth process of individual chains through incremental particle addition, enabling precise calculation of the key tangent angles that dictate chain structures. Visual representations of the final assembled structures enhance intuitive comprehension of aggregation mechanisms.

Additionally, to explore the aggregation firsthand, in this paper, we develop an easy and inexpensive synthetic method for tuning the dimensional order of FeCo nanostructures and observe their progression from 0D nanoparticles to the formation of 1D nanochains and finally their aggregation into complex 3D networks. By varying the NaOH concentration during synthesis, the influence of dimensionality on FeCo could studied without the influence of variation of too many other parameters. Through these experiments, we observe that the formation of 1D chains - similar to those predicted by the WLC model - and the formation of 3D networks depends on the NaOH to metal precursor concentration ratio in the solution, which leads to a variation in nucleation and growth rates, and therefore particle concentration.

Furthermore, we perform Monte Carlo (MC) simulations to study how the assembled structure's morphology is governed by the number of MNPs, correlating with the experimental nucleation rate. Unlike conventional MC simulation algorithms, our model simulates a realistic colloidal synthesis process. It achieves this by initiating the simulation with a small number of particles and subsequently introducing a specified number of particles into the system at predetermined time intervals to simulate nucleation events. By adjusting the number and generation rate of MNPs, the simulation yields a diverse set of architectures, including single chains, branched chains, and networks. We validate our model by comparing its predictions with experimental data. By establishing connections between particle parameters and NaOH concentration, our model serves as a valuable design guide for future MNP self-assembly experiments.

Finally, magnetic measurements comparing the 0D, 1D, and 3D structures reveal differences between their remanent magnetizations and coercivities as a result of structural differences at the nanoscale. The as-synthesized FeCo 3D networks exhibit the highest remanent magnetization and coercivity and show promise for future applications, especially compared to FeCo 0D nanoparticles.

The paper is organized as follows: in the next section, we provide a description of the WLC model and MC algorithms employed in our computer simulations. Subsequently, we experimentally investigate the structural properties of FeCo structures under varying [OH]/[M] ratios, which correspond to changes in particle size and density. We then employ simulations to analyze their impact on aggregate dimensionality. Finally, the manuscript concludes with magnetic characterizations to preliminarily illustrate the benefits of fabricating magnetic nanostructures of various dimensionalities.

2 Models

Our simulations assumed monodisperse and magnetically hard cubes with a characteristic side length L. Each cube had a magnetic dipole moment m located at its center and oriented in the [100] crystallographic direction. The simulations were performed in a 2D setting.

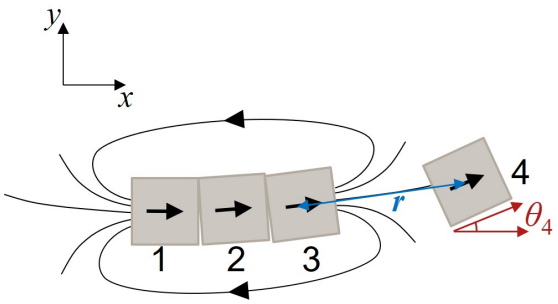

Fig. 1 Schematic illustration depicting the process of adding the 4^{th} particle to an existing chain in the WLC model.

2.1 WLC Model

A WLC model was utilized to investigate the dynamic growth of individual chains composed of N FeCo MNPs. As depicted in Fig. 1, we modeled a growth process by which individual cubes are added step by step, resulting in the formation of a chain composed of N cubes, each with the same magnetic moment m and side length L. The final chain morphology can be described by a set of N angles $\theta = \{\theta_1, ..., \theta_N\}$, representing the angles between each particle's [100] axis and that of the previous particle. The simulation begins with a single particle aligned along the x-axis ($\theta_1 = 0^\circ$) and incrementally adds particles until the total number reaches N.

For each new particle n to be added, a random difference angle $\Delta\theta$ is generated from a normal distribution with a one-sigma range of $[-30^\circ, 30^\circ]$ to represent its orientation relative to the previously added cube. In other words, the difference angle is $\Delta\theta = \theta_n - \theta_{n-1}$. The energy of the chain is then calculated assuming the particle gets added with this new angle θ_n. The energy associated with the chain follows the superposition of interaction energies, U, between the new cube and each cube on the existing chain, $E_n = \sum_{i=1}^{n-1} U_{n,i}$. The magnetic interaction energy U between two cubes inversely relates to the distance separating them, r, in free space (with permeability μ_0) as defined by:

$$U_{n,i} = -\frac{\mu_0 m^2}{2\pi r^3} \cos\Delta\theta_{n,i} \tag{1}$$

The probability P of attaching a new cube n to the existing chain takes the form of the Boltzmann distribution, comparing the energy of the chain E_n calculated assuming the newest angle θ_n, with the energy $E_{n,0}$ of the ground state chain arrangement having n particles.

$$P(\theta_n) = \frac{\exp\left[-\frac{E_n(\theta_n) - E_{n,0}}{k_b T}\right]}{\int_{-180^\circ}^{180^\circ} \exp\left[-\frac{E_n(\theta_n) - E_{n,0}}{k_b T}\right] d\theta_n} \tag{2}$$

In this expression, T is the temperature of the system, k_b is Boltzmann's constant, and $E_n(\theta_n)$ is the energy of the chain in a specific configuration θ_n. The ground state energy $E_{n,0}$ is calculated using the same Eq. (1), but for the case where all the particles in the chain are perfectly aligned, *i.e.*, $\theta = \{\theta_1, ..., \theta_N\} \equiv 0$. The denominator is the normalization factor for the probability distribution.

The probability $P(\theta_n)$ for the newly formed chain to adopt this particular configuration is calculated using Eq. (2), which is then compared to a randomly generated number lying between 0 and 1. If the random number is equal or smaller than the calculated probability $P(\theta_n)$, the particle is added to the chain, and the iteration proceeds to the next particle. The average cosine of the angles $\langle\cos\theta_n\rangle$ gives a sense for the overall shape of the chain and is computed over 100 simulations.

2.2 Monte Carlo Simulation

Since the MNPs exhibit vortex-like movement during the synthesis, we exclude other weak interactions like van der Waals forces, and focus specifically on the magnetic dipolar interactions. In our simulations, we establish a correlation between the experimental condition of [OH]/[M] concentration and the particle density D, as well as the particle generation rate $\dot{D}$. The total energy of the system E_{system} consisting of D particles is the summation of all of the particle interactions within the system:

$$E_{system} = \frac{\mu_0}{4\pi} \sum_{i \neq j}^{N} \left(\frac{m_i \cdot m_j}{r_{ij}^3} - 3\frac{(m_i \cdot \boldsymbol{r}_{ij})(m_j \cdot \boldsymbol{r}_{ij})}{r_{ij}^5} \right) \tag{3}$$

where m is the moment associated with a given particle denoted by its subscript (i or j), and $\boldsymbol{r}_{ij}$ and r_{ij} are the vector and magnitude of the distance between them, respectively. In this equation, the interaction energy is evaluated using the vectors between the particles in space as was done elsewhere[36], rather than the scalar form of the interaction in Eq. 1. At each iteration, a random trial movement on a random particle or a cluster of particles is tried, with a maximum displacement of $2L$ for the particle, and a maximum change in orientation of 180°. The total energy of the system is calculated using Eq. (3). If the perturbed state has a lower energy than the current state, the movement is accepted. To expedite convergence, we adopted a cluster-moving approach[37] and periodically checked for the formation of particle clusters. A cluster was deemed complete when the center-to-center distance between particles fell below a critical value of L. If a cluster formed, it was allowed to move and rotate rigidly around its center of mass.

3 Results and discussions

3.1 Experimental Observations

To evaluate the influence of NaOH concentration on the morphologies of the FeCo nanostructures, five sets of samples were prepared with varying ratios of NaOH to metal precursor concentration, [OH]/[M] = 50, 100, 120, 160, and 200, while keeping all other conditions the same. Table 1 lists the experiment conditions, final compositions, and structural morphologies of each of these FeCo alloy samples. The samples were denoted as S0, S1, S2, S3, and S4, respectively. Black powders were obtained from the aforementioned experiments. To ensure the suitability of our samples for future applications requiring magnetic alignment, we dropped cast them onto silicon wafer pieces under a weak magnetic field for both structural and magnetic characterizations. Additionally, electron microscope images of randomly-oriented samples were taken to validate their as-grown dimensionalities. The FESEM images of corresponding FeCo alloys are shown in Fig. 2. From low magnification FESEM images in the top row of Fig. 2, we note different densities of the same generic formation of long (tens of microns in length), narrow strands of FeCo structures along the direction of the applied magnetic field. The zoomed-in SEM images in the bottom row of Fig. 2 reveal that there are distinct differences in the structural dimensions of S0, S1, S2, S3, and S4. It is clear from the top row (low magnification) images, that the morphologies of S3 and S4 prevented them from spreading out into many separate strands across the surface, despite being the same total mass quantity as the other samples. As presented in the bottom row of high-magnification images of the 3D networks in Fig. 2d and e, FeCo chains are interlocked at different locations and with orientations along all three axes, producing a

porous 3D network structure. These structural linkages in the 3D network, help prevent the FeCo nanostructures from breaking apart and spreading out across the silicon wafer piece. FESEM and TEM images of samples drop-cast without a magnetic field are presented in Fig. 2f and Fig. S1, respectively. As shown, the FeCo nanoparticles (S0) exhibit a nearly cubic shape. The single-particle width, side-by-side aligned chains, and branched interconnected features are clearly distinguishable, representing 1D chains, bundled strands, and 3D network structures, respectively. Furthermore, unlike most previous studies of FeCo chains [18,19,38], there are no gaps among FeCo nanoparticles and the whole structures are purely metallic. Such an alloy system is expected to have good conductivity, which offers a potential advantage as bifunctional catalysts in energy applications [39].

The effect of NaOH concentration on the size of the FeCo nanoparticles has been reported previously [40], but the change in dimensional order has never been observed. As depicted in Fig. 2a, the FeCo 0D nanocubes were assembled into strands, and the widths were narrowly grouped about 450 nm in width, corresponding to 5 FeCo particles across. With the [OH]/[M] ratio increased from 50 to 100, chains with a width of single particle across can be observed (Fig. 2b). Although a few chains are stacked, the width of the strands in S1 is the narrowest among all samples. More FeCo alloy chains are interlaced and stacked to form chain bundles as the [OH]/[M] ratio increases to 120, representing the transition concentration regime between 1D chains and 3D networks. This interlacing effect is particularly evident at [OH]/[M] ratios higher than 120, which lead to a more interconnected 3D network in S3 and S4. It is clear that with increasing [OH]/[M] ratio, the dimensions of the FeCo structures change from 0D to 1D, and 3D, which will be discussed below. In our prior research [22], we explored the impact of a magnetic stirring bar employed during synthesis. Our findings revealed that self-assembled structures remain observable even without the presence of the stir bar. The rotational force, dependent on the stirring speed, has a far more pronounced impact on the self-assembled structure than the magnetic field generated by the stir bar. Therefore, at an optimal mixing speed, such as 300 rpm in this study, the rotational force becomes robust enough to efficiently disperse the particles, rendering the impact of the magnetic field from the stir bar on the assembly process negligible. Additionally, the similarity between the high saturation and remanent magnetizations (Table S1 in the Supporting Information) of *nanoparticles* in this study and those reported previously [41] further supports the conclusion that dipole-dipole interactions dominate in this work, as before, and that the magnetic effect of the stir bar can be disregarded during simulation and analysis of the assembly mechanisms.

The side length of the FeCo *nanoparticles* in S0 and the side length of the FeCo *chains* in the other samples were characterized and presented in Fig. 2f. The side lengths for all the samples are mostly within the range of 90 nm to 150 nm, while the widths of the bundled strands in Fig. 2 are significantly different. It is also evident that increasing the [OH]/[M] ratio could first increase and then decrease the size of the FeCo nanostructures. When [OH]/[M] $\leq$ 120, the side length increases with the NaOH molar concentration. Beyond that, the side length starts to decrease as the NaOH molar concentration continues to increase.

The crystal structure of the products was examined using XRD. Fig. 2h shows typical XRD patterns of the as-synthesized FeCo nanostructures for distinct [OH]/[M] ratios. The peaks can be assigned to the (110), (200), and (211) characteristic reflections of the body-centered cubic (bcc) FeCo alloy (JCPDS No. 49-1568), confirming the formation of highly crystalline products [42,43]. Scherrer analysis of the (110) plane shown in Fig. 2h yields an average crystallite size estimate of 30 nm across all samples, indicating that the FeCo structures are polycrystalline. As reported in Table 1, the final composition of $Fe_{100-x}Co_x$ nanostructures in all cases, determined by EDX, shows a slight deviation from that of the precursor concentration. All sample compositions were iron-rich compared to the initial precursor concentration, which is explained by the fact that iron is easier to be reduced compared with cobalt. However, based on the final compositions, it can be deduced that the rate of the cobalt reduction increases with increasing NaOH content. The sample synthesized with [OH]/[M] = 200 was in close agreement with the initial precursor concentration. The EDX elemental mappings for S0, S1, S2, S3 and S4 are presented in Fig. S2 in the Supporting Information. As expected, both elements, Fe and Co, are uniformly distributed in the 0D nanoparticle, 1D chain, and 3D network structures.

3.2 Simulations Results

To replicate the structural morphology shown in the bottom row of Fig. 2b, we conducted WLC simulations with a chain consisting of 20 cubes. Each cube, with a side length (L) of 140 nm, possesses a net magnetization along the edge (x-axis), as determined through our micromagnetic simulation detailed in our previous paper [22]. As shown in Fig. S3, the spin state at equilibrium was simulated, and the net magnetization was calculated as the vector sum of the local moments and found to be 1938 emu/cc. The direction of the net magnetization is inclined at an angle of 0.05° from the x-axis, which we approximated as being effectively aligned along x for the purposes of simplifying the simulation. The WLC simulations were performed using different values of k_bT, from 1×10^{-17} J to 1×10^{-14} J, empirically representing random environmental agitation. Fig. 3 depicts the cosine of the tangent angle $\cos\theta$ as a function of the particle's position along the chain, representing its propagation. Our observations reveal interesting trends depending on the position of MNPs and the k_bT value. For cases when the chain is short (less than 8 MNPs), regardless of the k_bT values, the $\cos\theta$ falls within the approximate range of [0.9, 1]. This suggests a high degree of alignment within the chain. However, as the number of MNPs surpasses 12, we noted a transition in the tangent angles and a divergence between those associated with small and larger k_bT values. Specifically, when the k_bT value is increased , the $\cos\theta$ of the added particle transitions from approximately 0.9 to 0.8. This indicates a decrease in alignment as the thermal energy becomes more significant.

To enhance the understanding of the data presented in Fig. 3,

Table 1 Synthesis and structural characterization of FeCo alloy nanostructures.

Sample	[OH]/[M]	Morphology	Initial composition (at.%)	Final composition (at.%)
S0	50	0D particles	$Fe_{50}Co_{50}$	$Fe_{65}Co_{35}$
S1	100	1D chains	$Fe_{50}Co_{50}$	$Fe_{62}Co_{38}$
S2	120	1D chain bundles	$Fe_{50}Co_{50}$	$Fe_{62}Co_{38}$
S3	160	3D networks	$Fe_{50}Co_{50}$	$Fe_{58}Co_{42}$
S4	200	3D networks	$Fe_{50}Co_{50}$	$Fe_{55}Co_{45}$

we provide a visual representation of the resulting chain configuration composed of 20 cubes under zero magnetic field. It can be observed that all the chains exhibit a deviation either towards the $+y$ or $-y$ direction when the chain is composed of more than 8 cubes. This deviation can be attributed to the magnetic behavior, where a slight initial deviation in the magnetic dipole direction from the second cube onwards continuously reinforces the deviation towards that direction. It is important to note that the specific structure of the 1D chains is highly dependent on the values of k_bT. At $k_bT = 1 \times 10^{-17}$ J, the chain can be accurately represented by a straight line, indicating a significant alignment of the nanocubes along the easy axis, which corresponds to the crystallographic axis [100]. As a result, the assembled structure appears linear. As k_bT increases to 1×10^{-16} J, although most of the cubes still lie approximately on the same line, some of them deviate slightly from the line. When k_bT continues to increase, the configuration of the chain undergoes a transition to a more zigzagged form, where individual particles deviate from the main axis of the chain, making it impossible to approximate the chain as a straight line. This structural variation is influenced by the interplay between the strength of dipole-dipole interactions and thermal energy, which changes with varying k_bT values. The dipole forces exerted on the MNPs cause the magnetization of each newly added particle to align with the existing chain, while the thermal energy acts in all directions equally. At lower temperatures, thermal fluctuations are not sufficient to overcome the magnetic dipole interaction. However, at higher temperatures, the dominance of thermal energy allows it to surpass the magnetic interaction energy, leading to increased deviations in the chain configuration.

The acceptance rate of a particle attaching to an existing chain was computed as a function of the particle's distance from the chain, assuming a particle size of $L = 140$ nm and k_bT value of 1×10^{-15} J. The results are presented in Supplementary Information Fig. S4, where error bars represent the variation in acceptance rates as a function of chain length. At each separation distance, r, between a new particle and an existing chain, the acceptance rate was simulated for cases when the existing chain has between 1 and 19 particles. Each data point represents the mean and standard deviation of these cases. Regardless of the existing chain length to which the new particle is being added, the curve demonstrates a clear overall trend: there is a steep decline in the acceptance rate as the separation distance, r, between the particle and the existing chain increases. At larger separation distances, the curve levels off, reaching a plateau once the separation distance surpasses a certain threshold. Upon closer examination, it is observed that the acceptance rate reaches its minimum and remains relatively unchanged when the separation distance corresponds to approximately 15 times the particle size ($15L$). This behavior can be attributed to the diminishing strength of the magnetic dipole interactions between the existing chain and new particle as a function of their separation distance, allowing for thermal agitation to separate them permanently and prevent the attachment.

Though the individual chain structure is defined by the probability of particles attaching with their given angular orientation, the morphology of the overall system and its dimensional order depends on the concentration of these particles. In experimental scenarios, when particles are positioned at a significant distance from each other, they tend to remain isolated. However, as the particles approach each other, the magnetic interactions between them become stronger. This increased magnetic force compels the particles to form chains or aggregate together to form more complex 3D structures.

To investigate the impact of the [OH]/[M] ratios on the equilibrium structure of the FeCo assemblies, we conducted MC simulations focusing on two particle parameters influenced by this experimental condition: the particle density D and the particle generation rate $\dot{D}$. For each [OH]/[M] ratio, the simulation was initialized with MNPs of size L and an initial particle count of 20. To simulate the synthesis process, we systematically introduced additional particles to the system at predefined intervals, $\dot{D}$, until the total number of MNPs in the state reached D. Depending on the [OH]/[M] ratio, the simulations were performed with varying total number of cubes (D = 150, 300, 360, 480, and 600) and particle generation rates ($\dot{D}$ = 4 per either 60, 50, 40, 30, and 20 iterations). Fig. 4a-c are the computational results at different iteration times (i = 0, 5000, 10000, and > 15000) for varying numbers of MNPs.

In a simulation illustrating the 0D case (D = 150), as the number of iterations increases (indicating the progression of reaction time), as shown in Fig. 4a, only an increase in the number of particles is observed, and no linear structures are formed. This phenomenon can be attributed to the low ratio of [OH]/[M], indicating a small quantity of nuclei. At D = 300 (Fig. 4b), early-stage assembly primarily resulted in the formation of small linear structures such as dimers or trimers. These structures had the potential to grow longer by absorbing nearby particles or merging with other dimers. As the number of particles increased to 300, some clusters gradually transformed into long chains over time. However, due to the low particle density, the assembled structures remained predominantly isolated linear structures. At a higher particle density of D = 360, as depicted in Fig. 4c, the aggregates formed at the early stage exhibited similar structures to those ob-

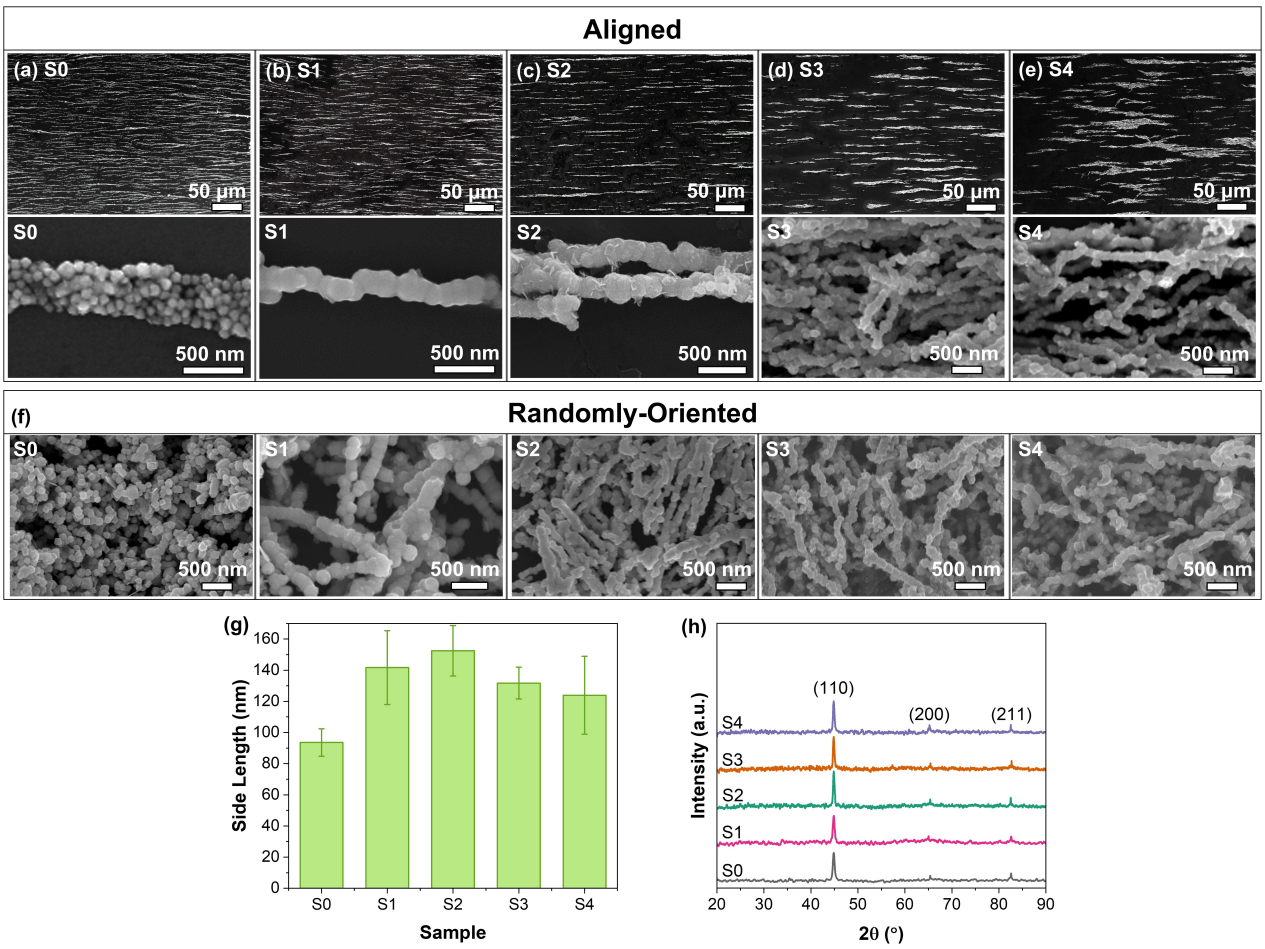

Fig. 2 FESEM images for samples synthesized under different [OH]/[M] ratios and different magnifications. [OH]/[M] = (a) 50, (b) 100, (c) 120, (d) 160, and (e) 200. (f) FESEM images of randomly-oriented samples. (g) Side length of the FeCo nanostructures synthesized at different [OH]/[M] ratios. S0: 50, S1: 100, S2: 120, S3: 160, and S4: 200. Side lengths are measured to be those of the *nanoparticles* in S0 and those of the *chains* in the other samples. (h) XRD patterns of the FeCo nanostructures synthesized at different [OH]/[M] ratios. S0: 50, S1: 100, S2: 120, S3: 160, and S4: 200. (110), (200), and (211) peaks correspond to the characteristic reflections of the body-centered cubic (bcc) FeCo alloy (JCPDS No. 49-1568).

served at low density (Fig. 4b). However, notable differences emerged at later stages. The higher particle density led to sets of neighboring linear chains aligning almost uniformly across the entire panel and eventually begin to stack into bundled strands. When the particle density increased to 480, the resulting structures in Fig. 4d showed exhibited chains that stacked upon each other, with a few branches crossing and forming interconnected networks. As anticipated, at a particle density of $D = 600$, compared to $D = 480$, a greater presence of branches was observed, indicating a more pronounced 3D network structure. Overall, the simulation results closely align with the experimental findings, accurately replicating the structures observed in samples S0, S1, S2, S3, and S4.

3.3 Comparison with Experiments

The simulation results obtained with $k_bT = 1 \times 10^{-15}$ J exhibit excellent agreement with the observed morphology of S1 as shown in the SEM image in Figure 2b. Both the experimental findings and simulation results reveal the presence of two-particle blocks or three-particle blocks that are slightly offset from the center line of the main chain. However, overall, the chain maintains an approximate straight configuration. In order to delve deeper into the relationship between the size of MNPs and the resulting chain morphology, we performed additional simulations with particle sizes of $L = 120$, 130, and 150 nm. Fig. S5 presents the corresponding $\langle \cos\theta \rangle$ and chain geometries versus the size of MNPs as a function of the number of MNPs under $k_bT = 1 \times 10^{-15}$ J. For less than 6 cubes, the geometries of chains composed of different-sized cubes exhibit similar structure, with only a slight increase in θ as the cube size is decreased. This suggests that the particle size has a negligible effect on the chain alignment in short chains. However, in longer chains, the size of MNPs becomes a significant factor, as smaller particles exhibit smaller $\langle \cos\theta \rangle$ (*i.e.*, larger θ) compared to the larger nanoparticles. This observation suggests that the size of the MNPs influences the degree of alignment within the chain, with smaller particles exhibiting more pronounced deviations from the main chain axis because the lower total volume and magnetic moment participating in the magnetic interaction makes it weaker. Additionally, for MNPs with size larger than 130 nm, there are no significant variations in $\langle \cos\theta \rangle$, suggesting that the dipolar interactions remain relatively strong under these conditions. Conversely, in the case of

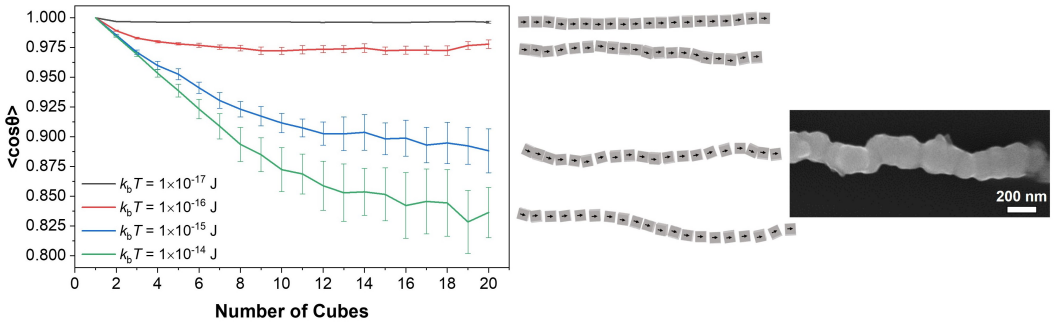

Fig. 3 Simulated $\langle \cos\theta \rangle$ results as a function of number of MNPs with particle size $L = 140$ nm and different k_bT values. The middle panel presents 3D rendering of chains corresponding to each k_bT value in the graph. The SEM image on the right shows the morphology of a synthesized chain having side length $L = 140$ nm and seeming to match the $\langle \cos\theta \rangle$ results for $k_bT = 1 \times 10^{-15}$ J. The yellow square outline aids in identifying each nanoparticle.

smaller nanoparticles ($L = 120$ nm), the $\langle \cos\theta \rangle$ values consistently remain below 0.85, suggesting that thermal energy is comparable to the magnetic interaction. A series of simulated chain geometries are also presented in Fig. S5. In summary, larger particle size leads to an increase in magnetic moment, resulting in stronger dipolar interactions and a higher likelihood of forming linear structures. However, once the particle size exceeds a certain threshold where magnetic dipole interactions become stronger than thermal fluctuations, further increases in size do not significantly affect the chain structure.

Both experiments and simulations have provided evidence of the significant influence of MNP concentration on the resulting structural morphologies of assemblies. The correlation between an increasing [OH]/[M] ratio in experiments and an increasing particle density N in simulations can be explained through the following reaction mechanism. In the synthesis process, the NaOH molar concentration dictates the concentration of MNP that are formed and how they grow. There are two stages during the reaction: nucleation and growth. In both processes, ethylene glycol first reduces the Fe^{2+} and Co^{2+} complexes into Fe and Co atoms with the assistance of NaOH. Subsequently, these atoms either nucleate to form a new particle core or grow on the surface of an existing particle core. When the NaOH molar concentration is low ([OH]/[M] $\leq$ 120), the freshly reduced atoms tend to grow on existing particles, which increases the side length of the FeCo structures. As schematically illustrated in Fig. S6, when the NaOH concentration in the ethylene glycol solution is significantly increased, the reduction rate is accelerated and the precursors tend to form additional new nuclei instead of growing on previous particles, which leads to the formation of more complex, higher dimensional-order FeCo structures. Increasing the NaOH concentration beyond this point would further speed up mass transfer and crystal growth.

In the 1D or 3D FeCo nanostructure synthesis case, high NaOH concentration provides the additional driving force for crystallographical fusion of isolated nanocrystals into high-aspect-ratio nanostructures[44]. The nanoparticles attach to each other, probably driven by the Ostwald ripening mechanism, and subsequently assemble into a chain owing to the attractive magnetic dipole forces between the magnetic particles. Hence, the NaOH concentration plays a significant role in the formation of FeCo alloys with complex structures. In summary, a moderate intensity of [OH]/[M] is most appropriate for the synthesis of 1D FeCo alloys. Decreasing the NaOH concentration too much will slow down reaction rate and yield 0D FeCo nanoparticles. At very high NaOH concentrations, the FeCo chains tend to aggregate into 3D networks.

Furthermore, the concentration of the NaOH slightly affects the final elemental composition of the FeCo alloys. When the NaOH concentration is low, the reduction rate for the less reducible ion, Co^{2+}, is slow, and the final product becomes iron-rich. In contrast, when the NaOH concentration is sufficiently high, it accelerates the reduction of less reducible element by generating intermediates that are more easily reduced to zero-valence metal atoms[45]. Therefore, the final composition of the FeCo alloys synthesized at high [OH]/[M] ratio is consistent with the iron and cobalt initial precursor concentration ratios used in the synthesis process as indicated in Table 1.

3.4 Magnetic Properties

The dependence of the magnetization, M, on the applied magnetic field, H, along two orthogonal directions of the aligned nanostructures shown in Fig. 2 ($\parallel$ and $\perp$ with respect to the long axis) was measured at room temperature and shown in Fig. 5a-e. For each of the samples, S0, S1, S2, S3, and S4, the difference between the normalized magnetic hysteresis loops along the two orthogonal magnetic field directions indicates that all samples show anisotropic magnetic behavior with low coercivity and low saturation fields, which are typical characteristics of soft magnetic behavior. It should be noted that although the FeCo nanoparticles should have little to no anisotropy in their individual 0D form, Fig. 5a shows a moderate variation of the shape of the hysteresis curves along two directions, which results from the measurement assembly of the nanoparticles of S0 in the form of elongated strands (as seen in Fig. 2). Nevertheless, the anisotropic magnetic behavior is less apparent for the 0D sample compared to the synthesized nanochains and nanoscale networks in samples S1-S4. As the dimensional order of the FeCo alloys increases from 0D to 1D to 3D, a larger variation in the shape of the loops is observed, indicating that dimensionality in these magnetic materials correlates with higher anisotropy (particularly from 0D to 1D) and overall higher magnetic coercivity.

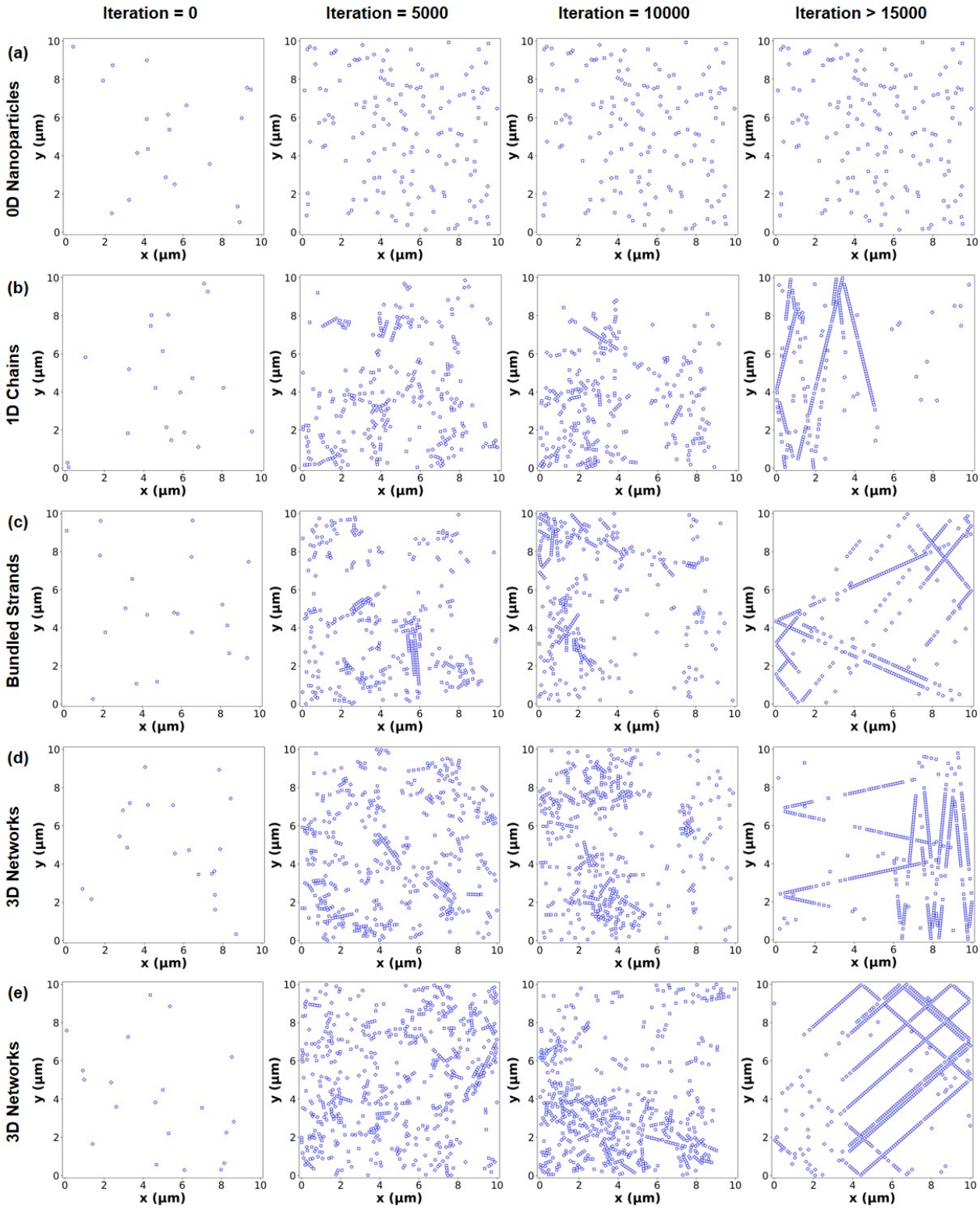

Fig. 4 Evolution of FeCo assemblies over time simulated with varying D values (D = a) 150, b) 300, c) 360, d) 480, and e) 600).

Table 2 Magnetic properties of FeCo alloy nanostructures.

Sample	Coercivity ($H_{C\parallel}$)	Coercivity ($H_{C\perp}$)	Normalized Remanence ($M_R/M_{S\parallel}$)	Normalized Remanence ($M_R/M_{S\perp}$)
S0	188.1 Oe	212.9 Oe	0.11	0.08
S1	122.4 Oe	157.0 Oe	0.21	0.07
S2	122.4 Oe	180.6 Oe	0.27	0.08
S3	148.5 Oe	208.5 Oe	0.30	0.10
S4	205.6 Oe	273.5 Oe	0.33	0.12

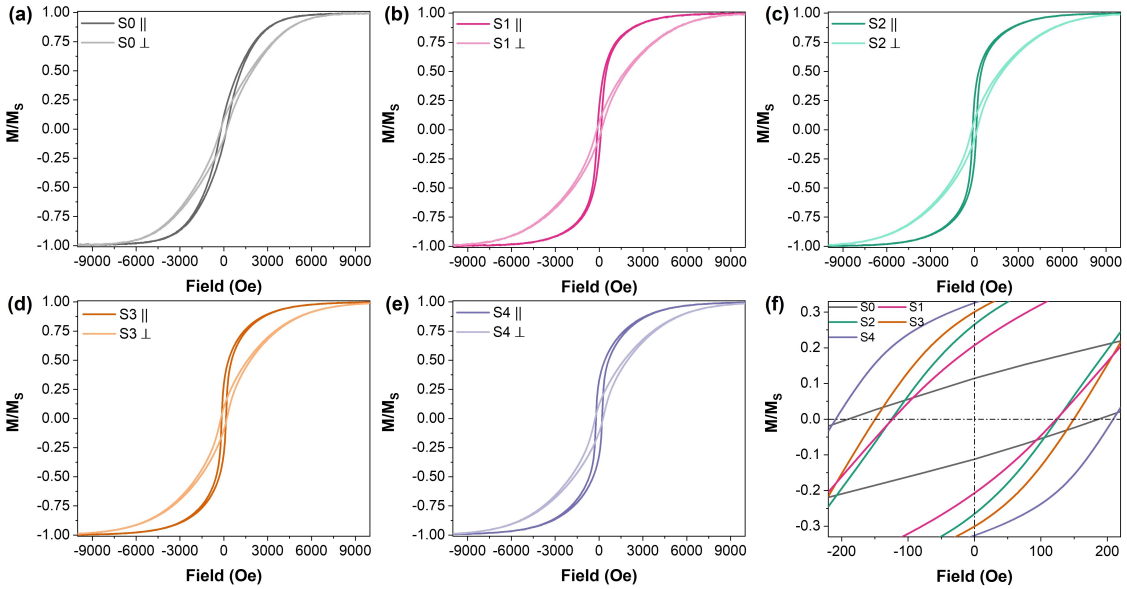

Fig. 5 (a) - (e) Magnetic hysteresis loops for samples measured with the external magnetic field applied parallel and perpendicular to the aligned axis of the samples in Fig. 2. (f) Zoomed-in loops for samples measured parallel to the external field.

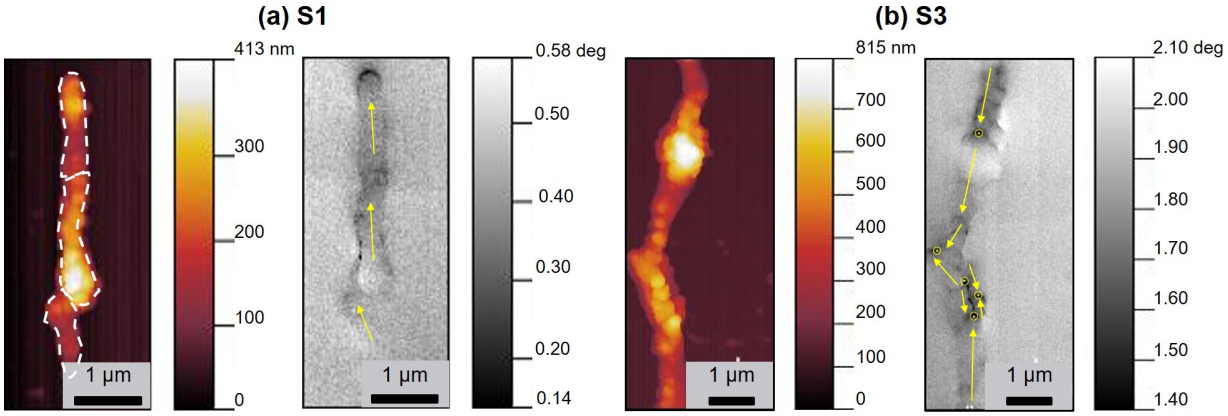

Fig. 6 The topological image (left), and the corresponding MFM micrograph (right) of the (a) S1: 1D chain and (b) S3: 3D network samples. Yellow arrows serve as guidelines to indicate the magnetic polarity of the structure.

Table 2 summarizes the $H_{C\parallel}$, $H_{C\perp}$, $M_R/M_{S\parallel}$, and $M_R/M_{S\perp}$ values for all the samples. The data shows a clear correlation between the structural and magnetic behavior. As the dimensional order increases, not only does the anisotropy increase, but this also translates to an increase in remanent magnetization; the 3D networks also see an increase in coercivity. Compared with other samples, S0 (synthesized at [OH]/[M] = 50) shows the lowest $M_R/M_{S\parallel}$ value. On the other hand, FeCo nanochains have an increased $M_R/M_{S\parallel}$ value owing to their anisotropic structure. With the synthesis of 3D FeCo structures, $M_R/M_{S\parallel}$ values is further increased.

The magnetic force microscopy (MFM) was utilized for further characterization. Panels a and b of Fig. 6 display topological and MFM images for the 1D chain and 3D network structures, respectively. The contrast variations in Fig. 6 correspond to the perpendicular components of the stray field, representing closure flux exiting the nanostructures and resulting from the magnetization. In Fig. 6a, the alternating dark and gray color contrast within the chain suggests the presence of three short chains that combine to form a longer chain with head-to-tail alignment. The darkest color at the topmost part of the long chain indicates the strongest out-of-plane flux (at the tip of the chain), while the less dark regions suggest weaker out-of-plane fringing fields (at points along the chain). This implies that the short chain in the middle is magnetically coupled with the chains above and below, resulting in predominantly in-plane magnetization. Conversely, in Fig. 6b, multiple dark points throughout the structure suggest significant out-of-plane magnetization in those locations, and indicate the likelihood of a complex domain structure and with multiple pinning points for domain walls within the 3D networks. This results from the fact that many smaller structures (particles and chains) are joined together at these points, with various orientations, each contributing a different flux configuration to the net field in that region.

The observed increase in $M_R/M_{S\parallel}$ with increasing dimensional order may be attributed to the unique morphology and complex magnetic domains present in these samples. This complexity likely causes an increase in coercivity due to a pinning of domain

walls at nodes of the network where nanochain-like structures intersect. Among all the samples, S1 (synthesized at [OH]/[M] = 100) and S2 (synthesized at [OH]/[M] = 120) showed the lowest $H_{C\|}$ values and S4 (synthesized at [OH/M] = 200) showing the highest. This might be attributed to the antiparallel dipolar coupling between adjacent chains.

All of these results provide strong evidence that the magnetic behavior of the FeCo alloys varies with the dimensional order of the structures. The 0D FeCo nanocubes exhibit low remanent magnetization, which could prevent particle agglomeration and makes it good candidate for biomedical applications. The unique anisotropic morphology of 1D FeCo chains would enable alignment of magnetic fillers in nanocomposites and allow enhancement in microwave absorption and electromagnetic interference shielding[46]. The 3D FeCo networked structures can be highly anticipated to hold great potential as advanced materials in electrocatalysis, due to high porosity, and neuromorphic computing, due to the complex networking[47,48].

4 Conclusions

In summary, we have presented the findings of a comprehensive experimental-computational study on magnetic FeCo assemblies. Our investigation involved examining the assembly behaviors of FeCo colloids across a wide range of [OH]/[M] ratios during synthesis. The results revealed a diverse array of self-assembled FeCo nanostructures, including 1D chains, bundled strands, and 3D networks. To achieve a deeper understanding, we conducted simulations that incorporated both the dynamic chain growth process and the colloidal synthesis process. Remarkably, these simulations demonstrated good agreement with experimental observations. Experimentally, the as-prepared FeCo nanochains and 3D networks show advantageous nanoscale magnetic properties of enhanced coercivity and remanent magnetization. Furthermore, the simplicity of adjusting the dimensional order of these structures in experiments opens up possibilities for their fabrication and utilization in various applications such as data storage devices, microelectronics, catalysis, and medicine. Future work can investigate the intricate spin texture and magnetization behavior inside these complex structures to better predict their complex magnetic behavior in a larger system.

Author Contributions

Yulan Chen: conceptualization, methodology, data analysis, original draft. Hanyu Alice Zhang: methodology, data analysis. Amal El-Ghazaly: funding acquisition, resources, supervision, validation, review and editing.

Conflicts of interest

There are no conflicts to declare.

Acknowledgements

The authors would like to express gratitude for the support received from the Cornell Center for Materials Research Shared Facilities, funded by the National Science Foundation (NSF) MRSEC program (DMR-1719875), and the Cornell NanoScale Facility, a member of the National Nanotechnology Coordinated Infrastructure (NNCI), which is generously supported by the NSF (Grant NNCI-2025233). This material is based upon work supported by the NSF under Grant No. 2030207. Any opinions, findings, and conclusions or recommendations expressed in this material are those of the authors and do not necessarily reflect the views of the National Science Foundation.

Notes and references

1 K. Deng, Z. Luo, L. Tan and Z. Quan, *Chemical Society Reviews*, 2020, **49**, 6002–6038.
2 M. Grzelczak, L. M. Liz-Marzán and R. Klajn, *Chemical Society Reviews*, 2019, **48**, 1342–1361.
3 G. Chen, K. J. Gibson, D. Liu, H. C. Rees, J.-H. Lee, W. Xia, R. Lin, H. L. Xin, O. Gang and Y. Weizmann, *Nature materials*, 2019, **18**, 169–174.
4 J. Yan, W. Feng, J.-Y. Kim, J. Lu, P. Kumar, Z. Mu, X. Wu, X. Mao and N. A. Kotov, *Chemistry of Materials*, 2019, **32**, 476–488.
5 Z. Ye, C. Li, Q. Chen, Y. Xu and S. E. Bell, *Nanoscale*, 2021, **13**, 5937–5953.
6 H. Soria-Carrera, E. Atrián-Blasco, J. M. de la Fuente, S. G. Mitchell and R. Martín-Rapún, *Nanoscale*, 2022, **14**, 5999–6006.
7 W. Wei, F. Bai and H. Fan, *Angewandte Chemie International Edition*, 2019, **58**, 11956–11966.
8 D. Liu, S. Li, T. Zhang, H. Jiang and Y. Lu, *ACS Applied Materials & Interfaces*, 2021, **13**, 36157–36170.
9 M. P. Arciniegas, A. Castelli, R. Brescia, D. Serantes, S. Ruta, O. Hovorka, A. Satoh, R. Chantrell and T. Pellegrino, *Small*, 2020, **16**, 1907419.
10 D. Li, Q. Xiong, D. Lu, Y. Chen, L. Liang and H. Duan, *Analytica Chimica Acta*, 2021, **1166**, 338567.
11 J. Mohapatra, J. Elkins, M. Xing, D. Guragain, S. R. Mishra and J. P. Liu, *Nanoscale*, 2021, **13**, 4519–4529.
12 M. P. Spencer, A. A. Alsaati, J. E. Park, R. B. Nogueira Branco, A. Marconnet and N. Yamamoto, *ACS Applied Materials & Interfaces*, 2022, **14**, 16601–16610.
13 P. W. Majewski, A. Michelson, M. A. Cordeiro, C. Tian, C. Ma, K. Kisslinger, Y. Tian, W. Liu, E. A. Stach, K. G. Yager *et al.*, *Science advances*, 2021, **7**, eabf0617.
14 M. Park, S. Kang, C. Nam, K. Narasimha, W. B. Lee and S.-J. Park, *ACS Applied Materials & Interfaces*, 2022, **14**, 8266–8273.
15 M. Varón, M. Beleggia, J. Jordanovic, J. Schiøtz, T. Kasama, V. F. Puntes and C. Frandsen, *Scientific Reports*, 2015, **5**, 1–7.
16 M. Hu, H.-J. Butt, K. Landfester, M. B. Bannwarth, S. Wooh and H. Thérien-Aubin, *ACS nano*, 2019, **13**, 3015–3022.
17 L. Balcells, I. Stanković, Z. Konstantinović, A. Alagh, V. Fuentes, L. López-Mir, J. Oró, N. Mestres, C. García, A. Pomar *et al.*, *Nanoscale*, 2019, **11**, 14194–14202.
18 E. Cui, F. Pan, Z. Xiang, Z. Liu, L. Yu, J. Xiong, X. Li and W. Lu, *Advanced Engineering Materials*, 2021, **23**, 2000827.
19 X. Zhang, Y. Li, R. Liu, Y. Rao, H. Rong and G. Qin, *ACS applied materials & interfaces*, 2016, **8**, 3494–3498.

20 R. M. Erb, H. S. Son, B. Samanta, V. M. Rotello and B. B. Yellen, *Nature*, 2009, **457**, 999–1002.

21 W. Li and Q. Li, *Nonlinear Dynamics*, 2018, **91**, 2141–2155.

22 Y. Chen and A. El-Ghazaly, *Small*, 2023, **19**, 2205079.

23 A. Fernández-Pacheco, R. Streubel, O. Fruchart, R. Hertel, P. Fischer and R. P. Cowburn, *Nature communications*, 2017, **8**, 1–14.

24 A. Fernández-Pacheco, L. Skoric, J. M. De Teresa, J. Pablo-Navarro, M. Huth and O. V. Dobrovolskiy, *Materials*, 2020, **13**, 3774.

25 B. Muzzi, M. Albino, C. Innocenti, M. Petrecca, B. Cortigiani, C. de Julián Fernández, G. Bertoni, R. Fernandez-Pacheco, A. Ibarra, C. Marquina *et al.*, *Nanoscale*, 2020, **12**, 14076–14086.

26 J. Richardi, M. Pileni and J.-J. Weis, *Physical Review E*, 2008, **77**, 061510.

27 R. Messina, L. Abou Khalil and I. Stanković, *Physical Review E*, 2014, **89**, 011202.

28 A. Wei, T. Kasama and R. E. Dunin-Borkowski, *Journal of materials chemistry*, 2011, **21**, 16686–16693.

29 J. G. Donaldson, P. Linse and S. S. Kantorovich, *Nanoscale*, 2017, **9**, 6448–6462.

30 J. G. Donaldson, P. Schall and L. Rossi, *ACS nano*, 2021, **15**, 4989–4999.

31 F. L. Durhuus, L. H. Wandall, M. H. Boisen, M. Kure, M. Beleggia and C. Frandsen, *Nanoscale*, 2021, **13**, 1970–1981.

32 A. U. Mahmood and Y. G. Yingling, *Journal of Chemical Theory and Computation*, 2022, **18**, 3122–3135.

33 L. J. Hill and J. Pyun, *ACS applied materials & interfaces*, 2014, **6**, 6022–6032.

34 M. B. Bannwarth, S. Utech, S. Ebert, D. A. Weitz, D. Crespy and K. Landfester, *ACS nano*, 2015, **9**, 2720–2728.

35 X. Xu and Y. Jiang, *International Journal of Modern Physics B*, 2018, **32**, 1840006.

36 J. Richardi, *Nanomaterials and Nanochemistry*, Springer, 2008, pp. 515–528.

37 G. Bertoni, B. Torre, D. Fragouli, A. Athanassiou and R. Cingolani, *The Journal of Physical Chemistry C*, 2011, **115**, 7249–7254.

38 M.-S. Jang, M. S. Chang, Y.-t. Kwon, S. Yang, J. Gwak, S. J. Kwon, J. Lee, K. Song, C. R. Park, S. B. Lee *et al.*, *Nanoscale*, 2021, **13**, 12004–12016.

39 G. Fu, Y. Liu, Y. Chen, Y. Tang, J. B. Goodenough and J.-M. Lee, *Nanoscale*, 2018, **10**, 19937–19944.

40 N. M. Lam, T. M. Thi, P. T. Thanh, N. H. Yen and N. H. Dan, *Physica B: Condensed Matter*, 2018, **532**, 71–75.

41 Y. Chen, K. Srinivasan, M. Choates, L. Cestarollo and A. El-Ghazaly, *Advanced Functional Materials*, 2024, **34**, 2305502.

42 Y. Yang, C. Xu, Y. Xia, T. Wang and F. Li, *Journal of Alloys and Compounds*, 2010, **493**, 549–552.

43 X. Li, B. Yang, X. Yang, Y. Cao and R. Yu, *Journal of Superconductivity and Novel Magnetism*, 2016, **29**, 417–422.

44 J. Jia, C. Y. Jimmy, X.-M. Zhu, K. M. Chan and Y.-X. J. Wang, *Journal of colloid and interface science*, 2012, **379**, 1–7.

45 F. Fiévet, S. Ammar-Merah, R. Brayner, F. Chau, M. Giraud, F. Mammeri, J. Peron, J.-Y. Piquemal, L. Sicard and G. Viau, *Chemical Society Reviews*, 2018, **47**, 5187–5233.

46 J. C. Sun, Z. He, W. Dong, W. Wu and G. Tong, *Journal of Alloys and Compounds*, 2019, **782**, 193–202.

47 L. Skoric, C. Donnelly, A. Hierro-Rodriguez, M. A. Cascales Sandoval, S. Ruiz-Gómez, M. Foerster, M. A. Niño, R. Belkhou, C. Abert, D. Suess *et al.*, *ACS nano*, 2022, **16**, 8860–8868.

48 C. Donnelly, A. Hierro-Rodríguez, C. Abert, K. Witte, L. Skoric, D. Sanz-Hernández, S. Finizio, F. Meng, S. McVitie, J. Raabe *et al.*, *Nature nanotechnology*, 2022, **17**, 136–142.